

Showcasing research from Dr Ke's laboratory, College of Chemistry and Chemical Engineering, Anhui University of Technology, Maanshan, Anhui, P. R. China.


Spontaneous generation of singlet oxygen on microemulsion-derived manganese oxides with rich oxygen vacancies for efficient aerobic oxidation

N_{55} - MnO_2 nanocatalysts with oxygen vacancy concentrations as high as 51.1% can be obtained by strategically incorporating defect engineering and interstitial N using compartmentalized-microemulsion crystallization followed by post-calcination. This feature allows the nanocatalyst to expose a substantial number of O_v and interstitial N sites on the surface of N_{55} - MnO_2 , facilitating effective chemisorption and activation of O_2 . As a result, the N_{55} - MnO_2 nanocatalyst enables room-temperature aerobic oxidation of alcohols with a yield surpassing 99%, representing a 6.7-fold activity enhancement compared to ϵ - MnO_2 without N-doping.

As featured in:



See Chao Wan, Qingping Ke, Yunqing Kang, Yusuke Yamauchi *et al.*, *Chem. Sci.*, 2023, **14**, 13402.

Cite this: *Chem. Sci.*, 2023, 14, 13402 All publication charges for this article have been paid for by the Royal Society of Chemistry

Spontaneous generation of singlet oxygen on microemulsion-derived manganese oxides with rich oxygen vacancies for efficient aerobic oxidation†

Jun Tang,^{ab} Junbao Chen,^a Zhanyu Zhang,^a Qincheng Ma,^a Xiaolong Hu,^a Peng Li,^a Zhiqiang Liu,^a Peixin Cui,^c Chao Wan,^{*de} Qingping Ke,^{*a} Lei Fu,^e Jeonghun Kim,^f Takashi Hamada,^g Yunqing Kang^{*e} and Yusuke Yamauchi^{*fgh}

Developing innovative catalysts for efficiently activating O_2 into singlet oxygen (1O_2) is a cutting-edge field with the potential to revolutionize green chemical synthesis. Despite its potential, practical implementation remains a significant challenge. In this study, we design a series of nitrogen (N)-doped manganese oxides ($N_y\text{-MnO}_2$, where y represents the molar amount of the N precursor used) nanocatalysts using compartmentalized-microemulsion crystallization followed by post-calcination. These nanocatalysts demonstrate the remarkable ability to directly produce 1O_2 at room temperature without the external fields. By strategically incorporating defect engineering and interstitial N, the concentration of surface oxygen atoms (O_s) in the vicinity of oxygen vacancy (O_v) reaches 51.1% for the $N_{55}\text{-MnO}_2$ nanocatalyst. This feature allows the nanocatalyst to expose a substantial number of O_v and interstitial N sites on the surface of $N_{55}\text{-MnO}_2$, facilitating effective chemisorption and activation of O_2 . Verified through electron paramagnetic resonance spectroscopy and reactive oxygen species trapping experiments, the spontaneous generation of 1O_2 , even in the absence of light, underscores its crucial role in aerobic oxidation. Density functional theory calculations reveal that an increased O_v content and N doping significantly reduce the adsorption energy, thereby promoting chemisorption and excitation of O_2 . Consequently, the optimized $N_{55}\text{-MnO}_2$ nanocatalyst enables room-temperature aerobic oxidation of alcohols with a yield surpassing 99%, representing a 6.7-fold activity enhancement compared to $\varepsilon\text{-MnO}_2$ without N-doping. Furthermore, $N_{55}\text{-MnO}_2$ demonstrates exceptional recyclability for the aerobic oxidative conversion of benzyl alcohol over ten cycles. This study introduces an approach to spontaneously activate O_2 for the green synthesis of fine chemicals.

Received 23rd August 2023
Accepted 9th October 2023

DOI: 10.1039/d3sc04418a

rsc.li/chemical-science

Introduction

Singlet oxygen (1O_2), recognized as a highly active and environmentally friendly reactive oxygen species (ROS), has garnered substantial attention from researchers in recent years.^{1–4} Benefiting from its remarkable oxidative capabilities and eco-friendliness, 1O_2 has found widespread applications in green catalysis,^{5–7} photocatalytic degradation,⁸ tumor diagnosis and treatment,⁹ and fluorescence probes.¹⁰ Nevertheless, the practical generation of 1O_2 typically necessitates intense photoexcitation due to the spin transition between ground and excited state molecular oxygen.¹¹ Throughout the last few decades, a range of photosensitizers, including photosensitive organic dyes,¹² organometallic complexes,¹³ and noble metals,^{14,15} have been devised to produce 1O_2 by harnessing photogenerated excitons and energy transfer pathways. However, the scarcity of noble metals and the susceptibility of organic photosensitizers to degradation render them inadequate to fulfill the escalating

^aCollege of Chemistry and Chemical Engineering, Anhui University of Technology, Maanshan 243002, Anhui, P. R. China. E-mail: Qingke@ahut.edu.cn^bSchool of Chemistry and Chemical Engineering, Shanxi University, Taiyuan 030006, P. R. China^cKey Laboratory of Soil Environment and Pollution Remediation, Institute of Soil Science, The Chinese Academy of Sciences, Nanjing 210008, P. R. China^dCollege of Chemical and Biological Engineering, Zhejiang University, Hangzhou 310058, P. R. China. E-mail: wanchao@zju.edu.cn^eResearch Center for Materials Nanoarchitectonics (MANA), National Institute for Materials Science (NIMS), 1-1 Namiki, Tsukuba, Ibaraki 305-0044, Japan. E-mail: yqkang@toki.waseda.jp^fDepartment of Chemical and Biomolecular Engineering, Yonsei University, 50 Yonsei-ro, Seodaemun-gu, Seoul 03722, South Korea^gDepartment of Materials Process Engineering, Graduate School of Engineering, Nagoya University, Nagoya 464-8603, Japan^hAustralian Institute for Bioengineering and Nanotechnology (AIBN), The University of Queensland, Brisbane, Queensland 4072, Australia. E-mail: y.yamauchi@uq.edu.au† Electronic supplementary information (ESI) available. See DOI: <https://doi.org/10.1039/d3sc04418a>

needs of green chemistry and sustainable development.^{11,16} Therefore, the construction of cost-effective and stable triggers for self-activating O₂ in a mild environment through catalyst innovation holds great significance.

Transition metal oxides are being considered as suitable candidates to replace noble metal catalysts due to their significant advantages, including low cost, excellent stability, and abundant reserves.^{17–20} Among these, manganese dioxides (MnO₂) stand out due to the multiple valence states and intricate electronic structures, which can be readily modified through structural-tailoring strategies to enhance their redox capabilities. Our previous studies have demonstrated the effectiveness of *in situ* heteroatom insertion techniques in producing highly active catalysts with ample oxygen vacancies (O_v).^{17,19} These O_v play a pivotal role in promoting the mobility of lattice oxygen (O_l), consequently enhancing oxidative capability through the Mars–Van Krevelen (MVK) mechanism, rather than inducing spontaneous O₂ transformation into ¹O₂.²¹ While theoretical studies have suggested that O₂ adsorbed on the surface of metal oxides can lead to the direct generation of ¹O₂, experimental breakthroughs in this area have been limited.^{22–24} Fortunately, the defect-engineering approach, particularly by modulating rich O_v, promotes the chemisorption of O₂, offering a promising avenue for activating O₂ to form ROS.^{25–31} For instance, the {111} facet of MgO, with its abundance of O_v, enables chemisorbed O₂ to undergo molecule transitions and electron rearrangements, resulting in the production of ¹O₂ even in the absence of light. However, the application in catalysis remains rarely explored.²⁴ It can be inferred that an increase in O_v content facilitates O₂ chemisorption on the surface of the catalyst, thereby promoting the formation of ¹O₂.^{24,25} These inspire us to devise catalysts with enhanced activity by creating ample surface chemisorption sites through innovative defect-engineering strategies.

The microemulsion composed of immiscible oleic and aqueous phases serves as a versatile platform for fabricating various nanocatalysts, distinguishing it significantly from conventional methods.^{32,33} Additionally, the utilization of microemulsions as templates for MnO₂ preparation offers unique advantages: (1) confined aqueous microdroplets create a conducive environment for effective heteroatom doping and the formation of abundant O_v; (2) uniformly sized MnO₂ nanocatalysts formed within these microdroplets tend to expose a higher proportion of surface O_v.^{32,33} However, the strategy of

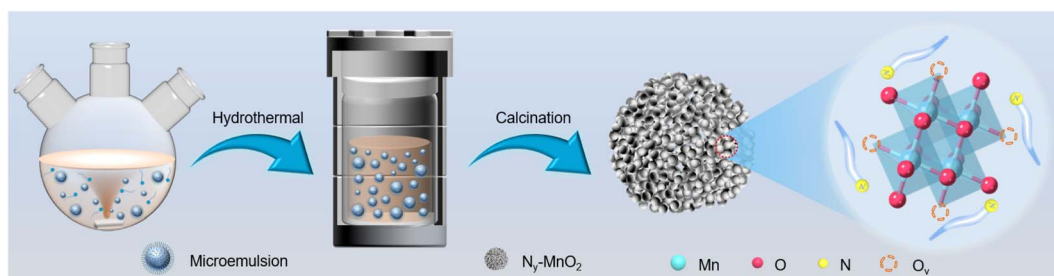
constructing high-concentration O_v based on a microemulsion microreactor is rarely reported.²⁵

In this study, we synthesized N-doped MnO₂ (N_y-MnO₂, where y represents the molar amount of urea used) nanocatalysts with adjustable O_v through crystallization within compartmentalized droplets of a microemulsion, followed by calcination. The resulting N_y-MnO₂ nanocatalysts are employed to activate O₂ and generate ¹O₂ for green oxidation processes. As demonstrated in the aerobic oxidation of benzyl alcohol, an important reaction pathway for the synthesis of fine chemicals, the catalytic activity of N₅₅-MnO₂ at room temperature significantly outperforms that of pristine ε-MnO₂ and commercially activated MnO₂ (C-MnO₂). We further elucidate how O_v promote O₂ chemisorption and spontaneous activation through structural characterizations and density functional theory (DFT) calculations. Moreover, the pivotal roles of ROS in the oxidation process through controlled quenching experiments are also verified. This work offers a practical strategy and theoretical insights for constructing environmentally friendly Mn-based catalysts and producing highly desirable ¹O₂ for efficient aerobic oxidation.

Results and discussion

Synthesis and characterization

Compartmentalized microemulsions, stabilized by an excess of surfactants, serve as versatile miniature reactors for the synthesis of N_y-MnO₂ to spontaneously produce ¹O₂ (Scheme 1). Within the confined aqueous microdroplets, isonitrile acid produced by urea decomposition reacts with Mn²⁺ to form catalyst precursor, manganese carbonate (MnCO₃), as verified by X-ray diffraction (XRD) patterns in Fig. S1a.† Fourier transform infrared (FTIR) spectra in Fig. S1b† display the presence of new peaks at 1443 cm^{−1}, 866 cm^{−1}, and 720 cm^{−1}, further confirming the successful formation of MnCO₃.^{33,34} Following calcination in air, MnCO₃ decomposes into MnO₂. The XRD patterns of the N_y-MnO₂ nanocatalysts, as shown in Fig. 1a, are identified as ε-MnO₂. The disappearance of the broad band at 1443 cm^{−1} and the emergence of peak at 1385 cm^{−1} in FTIR spectra indicates the incorporation of N atoms into ε-MnO₂ (Fig. S1b†). Additionally, X-ray photoelectron spectroscopy (XPS) was employed to analyze the embedded N in N₅₅-MnO₂. The distinct peak at 399.6 eV in the N 1s spectra of N_y-MnO₂ (Fig. 1b and S2†) is unequivocally attributed to N atoms inserted



Scheme 1 Schematic illustration of the preparation of N_y-MnO₂ nanocatalysts using compartmentalized microdroplets.



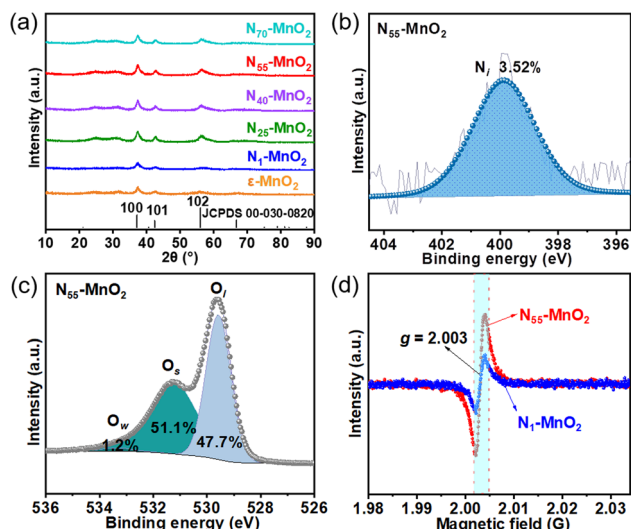


Fig. 1 (a) XRD patterns of N_y -MnO₂ ($y = 1, 25, 40, 55, 70$) and ϵ -MnO₂; (b) N 1s and (c) O 1s XPS spectra of N_{55} -MnO₂ (O_w : oxygen from water adsorption); (d) EPR spectra of N_1 -MnO₂ and N_{55} -MnO₂.

at interstitial sites.³⁵ The introduction of interstitial N minimizes the formation energy of O_v and facilitates the generation of high-concentration O_v .³⁵ As a result, the N_{55} -MnO₂ catalyst, with an optimal interstitial N content, achieves a maximum concentration of surface oxygen atoms (O_s) at 51.1% in the vicinity of O_v (Fig. 1c, S3, and Table S1†).^{36,37} In addition, the O_s content and the unsaturated Mn coordination (Mn^{3+}/Mn^{4+} ratio of 0.90, as shown in Fig. S4†), in N_{55} -MnO₂, significantly exceed that of similar catalysts (Table S2†).^{37–41} Furthermore, the evolutionary trend facilitated by interstitial N-doping is reflected in the increased-intensity peak of O_v at $g = 2.003$ in the electron paramagnetic resonance (EPR) spectrum in Fig. 1d. However, excessive N-doping in N_{70} -MnO₂ tends to occupy the formed vacancies, negatively affecting O_v formation (Fig. S3e†). As observed by transmission electron microscopy (TEM) in Fig. 2a, the N_{55} -MnO₂ catalyst possesses a size of ~ 115 nm, which is consistent with the results from dynamic light scattering (DLS,

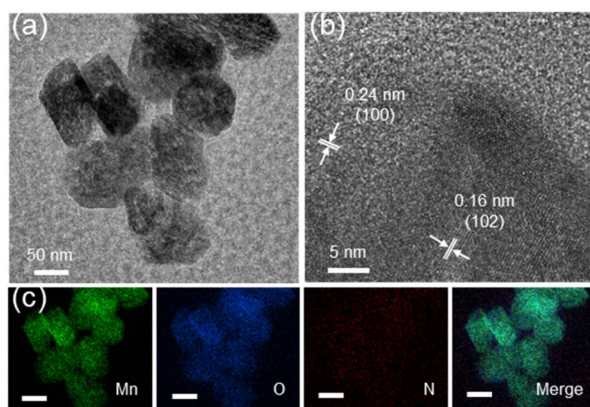


Fig. 2 (a) TEM, (b) HRTEM, and (c) EDS elemental mapping images (scale bars, 50 nm) of N_{55} -MnO₂ nanocatalyst.

Fig. S1c†). This demonstrates the distinctive compartmentalization effect of microemulsions in synthesizing uniform-size nanocatalysts. Additionally, High-resolution TEM (HRTEM) image of N_{55} -MnO₂ reveals d -spacings of 0.24 nm and 0.16 nm (Fig. 2b), corresponding to the (100) and (102) facets, respectively, of ϵ -MnO₂.⁴² Energy dispersive spectroscopy (EDS) element mapping images of N_{55} -MnO₂ demonstrate that interstitial N is uniformly embedded in the MnO₂ lattice (Fig. 2c). Doping interstitial N into MnO₂ leads to alterations in the original electronic structure and unsaturated coordination environment, thus enhancing the catalytic oxidation capacity.³⁷ This is confirmed through hydrogen temperature-programmed reduction (H_2 -TPR), with N_{55} -MnO₂ displaying the most prominent redox capability (Fig. S1d†), consistent with previous reports.^{37,43–47} Additionally, Brunauer-Emmett-Teller (BET) analysis of N_2 adsorption-desorption measurements was conducted to assess the BET parameters of N_y -MnO₂. As shown in Fig. S5 and Table S3,† N_{55} -MnO₂ exhibits the highest BET surface area of $78.7 \text{ m}^2 \text{ g}^{-1}$ among the N_y -MnO₂ samples and an average mesopore size of 11.41 nm. This can be attributed to the presence of O_v in N_y -MnO₂, which contribute to the formation of abundant mesopores on the surface of N_y -MnO₂.⁴⁸

Adsorption of O₂ and production of ¹O₂

Previous studies have demonstrated that an increased concentration of O_v enhances the chemical adsorption of O₂, leading to the elongation of the O–O bond and facilitating O₂ activation.^{24,25,48} Our DFT calculations reveal that the adsorption energy of O₂ on the surface of ϵ -MnO₂ is -1.24 eV, whereas it decreases to -2.18 eV on N_{55} -MnO₂ (Fig. 3a). This indicates that the augmented O_v resulting from N-doping reduces the adsorption energy of O₂, thereby promoting its chemisorption and excitation.²⁵ To gain further insights, we employed *in situ* IR spectroscopy for real-time monitoring of O₂ adsorption and activation on the surface of N_{55} -MnO₂. As shown in Fig. 3b, a chemisorption peak of O₂ emerges at 1401 cm^{-1} in an O₂ atmosphere, followed by the gradual formation of a robust band corresponding to surface-bonded superoxide anion species ($O_2^{\cdot-}$) at 1052 cm^{-1} .^{49,50} This illustrates the role of O_v in promoting O₂ activation. Conversely, no discernible peaks are observed under an O₂ + H₂O vapor atmosphere, possibly due to H₂O occupying the O_v and preventing O₂ adsorption (Fig. S6a†).

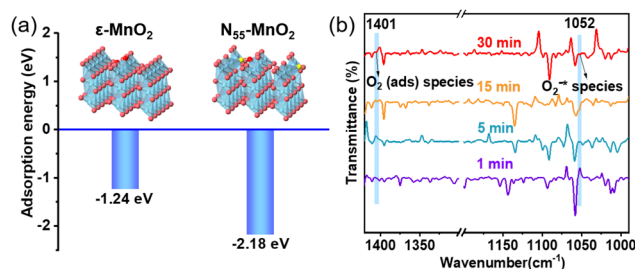


Fig. 3 (a) Adsorption energy of O₂ on the surface of pristine ϵ -MnO₂ and N_{55} -MnO₂ obtained by DFT calculation; (b) *in situ* IR spectra of O₂ adsorbed onto the surface of N_{55} -MnO₂.

The direct interactions between O_2 and N_y - MnO_2 were investigated without light irradiation using EPR. 2,2,6,6-tetramethylpiperidine (TEMP) was employed as a quencher to capture 1O_2 activated by N_y - MnO_2 at room temperature. As depicted in Fig. 4a and b, N_1 - MnO_2 , which exhibits fewer O_v , generates only $^{\bullet}O_2^-$ and not 1O_2 . With an increase in urea feeding, enhanced N-doping promotes O_v formation in N_y - MnO_2 . Notably, distinct triple peaks corresponding to $TEMP\text{-}^1O_2$ are evident for both N_{55} - MnO_2 and N_{25} - MnO_2 , with an intensity ratio of 1:1:1.²⁵ The intensity of the 1O_2 peak strengthens with higher O_v content, underscoring the significant role of O_v in activating O_2 . Quantitative EPR analysis indicates that N_{55} - MnO_2 generates 1O_2 at an average rate of $5.94 \text{ mol g}_{\text{cat}}^{-1} \text{ L}^{-1} \text{ min}^{-1}$ (Fig. 4c). Importantly, N_y - MnO_2 doesn't produce highly reactive hydroxyl radicals ($^{\bullet}OH$, Fig. S6†). To investigate the contribution of O_v to the excitation of O_2 , various ϵ - MnO_2 nanocatalysts were synthesized and characterized without N doping (Fig. S7–S9†). Interestingly, ϵ - MnO_2 -*n*-350 (where 350 indicates the thermal treatment temperature), with the highest O_s concentration of 44.4%, demonstrates the capability to generate 1O_2 under mild conditions (Fig. S10†). These findings underscore the pivotal role played by abundant surface-exposed O_v in nano-sized MnO_2 for the self-activation of O_2 . However, the catalytic activity of ϵ - MnO_2 -*n*-350 is still much lower than that of N_{55} - MnO_2 can be attributed to the doping effect of interstitial N, which will be further discussed later.

To investigate the roles of ROS in the reaction, controlled quenching experiments were conducted. As shown in Fig. 4d, the conversion of benzyl alcohol sharply decreases from >99.9% to 26% after the addition of TEMPO as a ROS quencher, indicating that ROS mediate the oxidative reaction. Upon separately introducing 1,4-benzoquinone (BQ) and isopropyl alcohol (IPA), the conversion of benzyl alcohol decreases slightly, illustrating that $^{\bullet}O_2^-$ and $^{\bullet}OH$ play subsidiary roles in the selective

oxidation process. Surprisingly, the oxidation reaction is nearly halted when furfuryl alcohol (FA) is used to capture 1O_2 . This undeniable evidence confirms 1O_2 as the primary ROS in this O_2 -mediated oxidative reaction. In summary, 1O_2 is spontaneously generated through the direct activation of O_2 , rather than the oxidation of $^{\bullet}O_2^-$ observed in photocatalytic processes.⁵² Despite O_2 being the source of ROS, the conversion of benzyl alcohol can be achieved at 31% and 25.5% under N_2 and Ar atmospheres, respectively (Fig. 4d, S11, and Table S4†). This is attributed to the involvement of O_1 in the aerobic oxidation process, following the MVK mechanism, which is consistent with previous reports.^{17,44}

Selective oxidation of alcohols

Aerobic oxidation of alcohols serves as a widely important model reaction for assessing the oxidative activity of the catalyst. However, effectively exciting O_2 with catalysts remains a challenge.^{15,20} If a catalyst can spontaneously generate 1O_2 from the ground-state oxygen, it will significantly advance the development of environmentally friendly catalysis. The plausible reaction process for efficient oxidation by N_y - MnO_2 is presented in Fig. 5. O_v and interstitial N sites promote O_2 adsorption on the surface of N_y - MnO_2 , while O_v elongate the O–O bonds, facilitating direct excitation of O_2 to 1O_2 for efficient alcohol oxidation. We evaluate the catalytic performance of N_y - MnO_2 for the aerobic oxidation of benzyl alcohol under O_2 bubbling conditions. We observe that micrometer-scale ϵ - MnO_2 displays low activity (conversion rate of 18.2% in 2.5 hours) due to its inability to activate O_2 to form 1O_2 (Fig. 6a and S10†). The C- MnO_2 exhibits negligible activity (Fig. S12 and S13†). In contrast, N_{55} - MnO_2 achieves 99.9% conversion and 99.9% selectivity in 2.5 hours, with a turnover frequency (TOF) 7.4 and 6.7 times higher than that of ϵ - MnO_2 and ϵ - MnO_2 -*n*-350, respectively (Fig. 6b and Table S5†).

To unravel the catalytic reaction mechanism, we conducted kinetics studies using various catalysts. It can be observed that the initial reaction rate remains constant under different O_2 pressures, indicating independence from O_2 pressure variations (Fig. S14 and Tables S6–S8†). Through calculation and fitting,

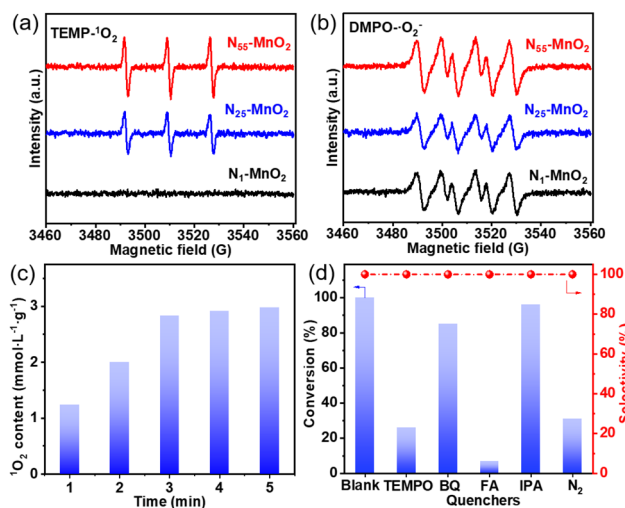


Fig. 4 The characteristic peaks of (a) $TEMP\text{-}^1O_2$ and (b) $DMPO\text{-}^{\bullet}O_2^-$ captured by EPR; (c) the content of 1O_2 produced by N_{55} - MnO_2 ; (d) the controlling experiment catalyzed by N_{55} - MnO_2 with different quenchers.

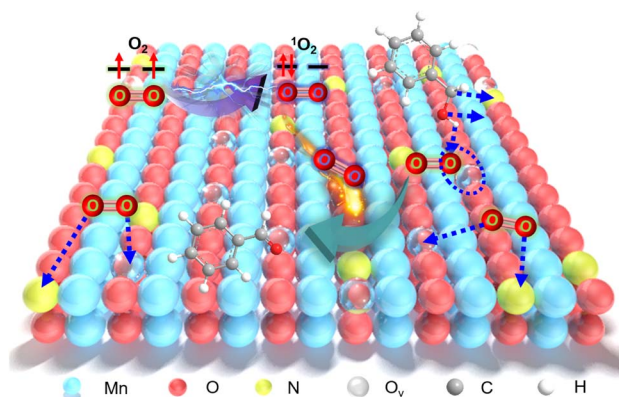


Fig. 5 Plausible reaction process for efficient oxidation by N_y - MnO_2 activating O_2 to form 1O_2 .



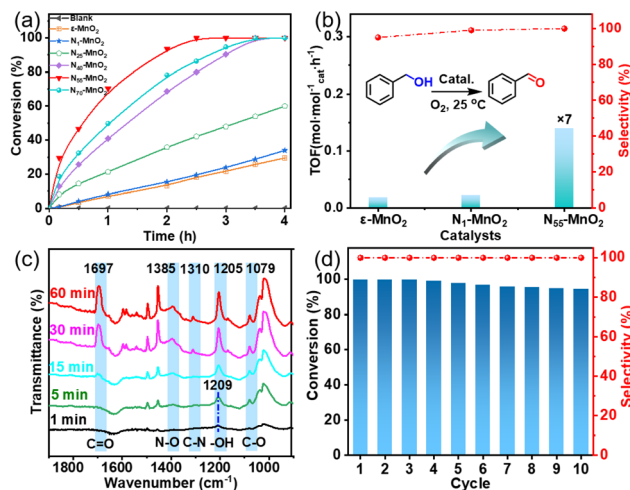


Fig. 6 (a) Aerobic oxidation of benzyl alcohol using activated ϵ -MnO₂ and N_y-MnO₂ ($y = 1, 25, 40, 55, 70$), (b) the comparison of TOF of ϵ -MnO₂, N₁-MnO₂, and N₅₅-MnO₂ (TOF = moles of benzyl alcohol converted per mole of catalyst/reaction time); (c) *in situ* IR spectra of oxidation of benzyl alcohol on the surface of N₅₅-MnO₂; (d) the recyclability of N₅₅-MnO₂ for aerobic oxidation of benzyl alcohol.

the reaction is found to be correlated with the concentration of benzyl alcohol, further demonstrating a first-order reaction (Tables S9 and S10[†]). Furthermore, we calculate the activation energies (E_a) of the N₁-MnO₂, N₂₅-MnO₂, and N₅₅-MnO₂ catalysts using the Arrhenius equation, resulting in values of 55.04 kJ mol⁻¹, 45.87 kJ mol⁻¹, and 43.17 kJ mol⁻¹, respectively (Fig. S15 and Tables S11–S13[†]). Evidently, the catalytic performance of N_y-MnO₂ is positively correlated with its O_v content, providing further evidence of the role of O_v in the oxidation process. *In situ* IR spectra were utilized to analyze the dynamic process of benzyl alcohol oxidation on the surface of N₅₅-MnO₂, revealing enhanced catalytic performance. Under an O₂ atmosphere, N₅₅-MnO₂ serves as the background for data acquisition. In the first five minutes, four characteristic peaks emerge in Fig. 6c. Compared with C-MnO₂ (Fig. S16[†]), the newly appeared N–O peak at 1385 cm⁻¹ on N₅₅-MnO₂ is attributed to O₂ adsorption by interstitial N sites. At 1310 cm⁻¹, the band corresponds to the stretching vibration of C–N bonds. The formation of C–N bonds is facilitated by the chemisorption of –OH groups from alcohol onto the interstitial N sites. After exposure to an O₂ flow for 15 minutes, the O–H band shifts from 1209 cm⁻¹ to 1205 cm⁻¹, indicating an interaction between the adsorbed O₂ species and –C–OH groups on benzyl alcohol. Continuing the exposure for 30 minutes, the broad C=O band at 1697 cm⁻¹ signifies the formation of benzyl aldehyde catalyzed by N₅₅-MnO₂.

Semiconductor catalysts have recently demonstrated an enhanced capacity for generating ¹O₂ when exposed to light, resulting in improved oxidation performance.^{24,25} In contrast, N₅₅-MnO₂ exhibits virtually unchanged activity under both light and dark conditions (Table S4[†]). This observation suggests that the inherent capability of N₅₅-MnO₂ to spontaneously generate ¹O₂ operates independently of external factors, marking

a significant difference from previously reported studies.^{25,50,53,54}

Compared to recently reported heterogeneous catalysts, the well-designed N_y-MnO₂ nanocatalysts display a unique ability to spontaneously generate sufficient ¹O₂ under mild reaction conditions. This enables the green and efficient conversion of alcohols without the need for light or additives, showcasing their superior catalytic activity (Table S14[†]).

Furthermore, we investigated the applicable substrate scope of aerobic oxidation. As shown in Table 1, aromatic primary alcohols, including benzyl alcohol and its derivatives, exhibit yields of over 99.9% for the corresponding aldehydes. Even for aromatic secondary alcohols, yields exceeding 99.9% are obtained when the reaction time extends to 6.0 hours. In comparison, the catalytic performance of N₅₅-MnO₂ in the oxidation of aliphatic alcohols (e.g., 1-hexanol) is hampered by significant

Table 1 Catalytic activity of N₅₅-MnO₂ for aerobic oxidation of various alcohols^a

$\text{R}_1-\text{CH}(\text{OH})-\text{R}_2 \xrightarrow[\text{O}_2, 25^\circ\text{C}]{\text{N}_{55}\text{-MnO}_2} \text{R}_1-\text{C}(=\text{O})-\text{R}_2$				
Entry	Product	Conv. (%)	Sel. (%)	Yield (%)
1		99.9	>99.9	>99.9
2		99.9	>99.9	>99.9
3		99.9	>99.9	>99.9
4		82.6	>99.9	>82.6
5		99.9	>99.9	>99.9
6		99.9	>99.9	>99.9
7		99.9	>99.9	>99.9
8		99.9	>99.9	>99.9
9		99.9	>99.9	>99.9
10 ^b		99.9	>99.9	30.5
11 ^b		99.9	>99.9	47.3
12		n.d.	—	n.d.

^a Reaction condition: 5.0 mL of toluene, 0.5 mmol of alcohols, 150.0 mg of N₅₅-MnO₂, 1200 rpm, 25.0 ± 1.0 °C, O₂ flow 16.0 mL min⁻¹ 1.0 bar, reaction time 2.5 h, n. d. not detect. ^b Reaction time 6.0 h.



steric hindrance effects. Using benzyl alcohol as the model substrate, we evaluate the recyclability of N_{55} - MnO_2 in aerobic oxidation. As depicted in Fig. 6d, N_{55} - MnO_2 maintains >94% conversion of benzyl alcohol and >99.9% selectivity toward aldehydes over ten cycles. Additionally, XRD and XPS characterizations confirm the stability of the recycled N_{55} - MnO_2 structure (Fig. S17†). To the best of our knowledge, results demonstrating both sufficient formation of 1O_2 and the green oxidation of alcohols under mild conditions have been scarcely reported.

Conclusions

In conclusion, we have successfully developed a range of N_y - MnO_2 nanocatalysts capable of directly generating 1O_2 at room temperature for the aerobic oxidation of alcohols. The *in situ* insertion of interstitial N into MnO_2 within encapsulated aqueous microreactors can lead to O_s concentrations of up to 51.1% for N_{55} - MnO_2 and enhance chemisorption of reactants. Consequently, these well-synthesized N_y - MnO_2 nanocatalysts have demonstrated enhanced redox performance due to their higher surface O_v exposure and N-doping. DFT calculations have revealed that the interstitial N and increased O_v content facilitates the chemisorption of O_2 , resulting in the generation of sufficient 1O_2 . Under aerobic oxidation conditions, the N_{55} - MnO_2 catalyst has achieved alcohol conversion rates exceeding 99.9% and aldehyde selectivity of over 99.9%, without the use of additives. Additionally, the N_{55} - MnO_2 catalyst has displayed a TOF value of $0.14 \text{ mol mol}_{\text{cat}}^{-1} \text{ h}^{-1}$, 6.7 times higher than that of the N-undoped ε - MnO_2 catalyst. Furthermore, N_{55} - MnO_2 has shown excellent catalytic stability after ten cycles, remaining robust even after recycling and calcination under an air atmosphere. This study introduces a strategy for fabricating efficient ROS triggers within compartmentalized microdroplets, resulting in the generation of favorable 1O_2 to facilitate the aerobic oxidation of alcohols.

Experimental

Synthesis of N_y - MnO_2 catalyst

A homogeneous oil phase was achieved through vigorous mechanical stirring of sodium dodecyl benzene sulfonate (10.5 g) and xylene (90 mL). Subsequently, a mixture containing manganese(II) nitrate tetrahydrate (10 mmol), water (5.4 mL), and urea (1, 25, 40, 55, 70 mmol) was gently introduced into the aforementioned oil phase, resulting in the formation of a water-in-oil (W/O) microemulsion. After stirring for 30 min, the resulting microemulsion was transferred to a 100 mL Teflon autoclave and hydrothermally treated at 160 °C for 8 h. Finally, the received gray precursor was dried overnight under vacuum, and heated at 350 °C in a muffle furnace to obtain N_y - MnO_2 catalyst, where y represents the molar amount of urea used.

Catalytic performance of aerobic oxidation

N_y - MnO_2 (150 mg), toluene (5 mL), and benzyl alcohol (0.5 mmol) were charged into a Schleck flask, and the temperature

was maintained at 25.0 ± 1.0 °C. The reaction mixture was stirred magnetically at 1200 rpm, while O_2 was continuously bubbled at a rate of 16 mL min^{-1} . After several hours of reaction, the mixture was analyzed by gas chromatography (PANNA A91Plus). The used N_y - MnO_2 was recycled by high-speed centrifugation and subsequently calcined at 350 °C for 4 h.

ROS trapping experiment

The ROS control experiments followed procedures similar to the aerobic oxidation process. In these experiments, benzyl alcohol and FA were employed as the model substrate and 1O_2 scavenger, respectively. N_y - MnO_2 (150.0 mg), toluene (5.0 mL), benzyl alcohol (0.5 mmol), and FA (1.0 mmol) were sequentially introduced into a reaction tube, maintaining the temperature at 25.0 ± 1.0 °C. The mixture underwent magnetic stirring (1200 rpm) with a continuous O_2 flow (16.0 mL min^{-1}). Upon completion of the reaction, the conversion of benzyl alcohol was assessed using gas chromatography. Additionally, experiments involving TEMPO, BQ and IPA quenchers were conducted following the aforementioned procedures. The roles of ROS (1O_2 , $\cdot O_2^-$ and $\cdot OH$) in oxidative reaction were analyzed based on the observed oxidation of benzyl alcohol.

Author contributions

J. T. and J. C.: conceptualization, methodology, writing – original draft. Y. Z. Q. M. and P. C.: chemical experiments and analysed the data. Y. K., L. F., J. K., and T. H. participated in various aspects of the experiments and discussions. X. H., P. L. and Z. L.: recycling experiments. C. W., Q. K., Y. K., and Y. Y. review & editing, supervision.

Conflicts of interest

There are no conflicts to declare.

Acknowledgements

Dr Y. K. thanks the support from JSPS Postdoctoral Fellowships for Research in Japan. This work was financially supported by the National Natural Science Foundation of China (22302001, 22108238), Key Projects of the Department of Education of Anhui Province of China (RZ2000003450, 2022AH050314), Anhui Provincial Natural Science Foundation of China (2008085MB47), the China Postdoctoral Science Foundation (2019M662060, 2020T130580, PC2022046), and Scientific Research Training Program for College Students of Anhui University of Technology (202110360040, S202110360213, S202310360207, 202310360037). This work was supported by the JST-ERATO Yamauchi Materials Space-Tectonics Project (JPMJER2003) and the UQ-Yonsei International Research Project. The authors would like to thank Zhengjie Chen and Zhangli Pei from SCI-GO (<https://www.sci-go.com>) for the EPR analysis. The authors also thank Shijianjia Lab (<https://www.shijianjia.com>) for the support of the XRD, XPS, and BET



tests. This work used the Queensland node of the NCRIS-enabled Australian National Fabrication Facility (ANFF).

References

- C. Lu, C. Zhang, P. Wang, Y. Zhao, Y. Yang, Y. Wang, H. Yuan, S. Qu, X. Zhang, G. Song and K. Pu, *Chem*, 2020, **6**, 2314–2334.
- C. Bloyet, F. Sciortino, Y. Matsushita, P. A. Karr, A. Liyanage, W. Jevasuwan, N. Fukata, S. Maji, J. Hynek, F. D'Souza, L. K. Shrestha, K. Ariga, T. Yamazaki, N. Shirahata, J. P. Hill and D. T. Payne, *J. Am. Chem. Soc.*, 2022, **144**, 10830–10843.
- X. Bao, H. Li, Z. Wang, F. Tong, M. Liu, Z. Zheng, P. Wang, H. Cheng, Y. Liu, Y. Dai, Y. Fan, Z. Li and B. Huang, *Appl. Catal., B*, 2021, **286**, 119885.
- X. Liu, H. Yu, J. Huang, J. Su, C. Xue, X. Zhou, Y. He, Q. He, D. Xu, C. Xiong and H. Ji, *Chem. Sci.*, 2022, **13**, 9560–9568.
- D. Kalaitzakis, A. Bosveli, K. Sfakianaki, T. Montagnon and G. Vassilikogiannakis, *Angew. Chem., Int. Ed.*, 2021, **133**, 4381–4387.
- W. Wu, C. Han, Q. Zhang, Q. Zhang, Z. Li, D. J. Gosztola, G. P. Wiederrecht and M. Wu, *J. Catal.*, 2018, **361**, 222–229.
- Q. Ke, S. Fang, J. Tang, F. Li, C. Ning, Z. Tang, Q. Ling, X. Liu and P. Cui, *ChemPhotoChem*, 2022, **6**, e202200075.
- L. Kong, G. Fang, X. Xi, Y. Wen, Y. Chen, M. Xie, F. Zhu, D. Zhou and J. Zhan, *Chem. Eng. J.*, 2021, **403**, 126445.
- H. Ma, S. Long, J. Cao, F. Xu, P. Zhou, G. Zeng, X. Zhou, C. Shi, W. Sun, J. Du, K. Han, J. Fan and X. Peng, *Chem. Sci.*, 2021, **12**, 13809–13816.
- C. Lin, S. M. Bachilo and R. B. Weisman, *J. Am. Chem. Soc.*, 2020, **142**, 21189–21196.
- R. Gao, X. Mei, D. Yan, R. Liang and M. Wei, *Nat. Commun.*, 2018, **9**, 2798.
- N. Singh, P. Kumar, R. Kumar and U. Riaz, *Ind. Eng. Chem. Res.*, 2019, **58**, 14044–14057.
- Y. Chen, Z. Wang, H. Wang, J. Lu, S. Yu and H. Jiang, *J. Am. Chem. Soc.*, 2017, **139**, 2035–2044.
- R. Long, K. Mao, X. Ye, W. Yan, Y. Huang, J. Wang, Y. Fu, X. Wang, X. Wu, Y. Xie and Y. Xiong, *J. Am. Chem. Soc.*, 2013, **135**, 3200–3207.
- J. Huang, S. He, J. L. Goodsell, J. R. Mulcahy, W. Guo, A. Angerhofer and W. D. Wei, *J. Am. Chem. Soc.*, 2020, **142**, 6456–6460.
- W. Zhang, W. Huang, J. Jin, Y. Gan and S. Zhang, *Appl. Catal., B*, 2021, **292**, 120197.
- J. Tang, Y. Cao, F. Ruan, F. Li, Y. Jin, M. N. Ha, X. Han and Q. Ke, *Ind. Eng. Chem. Res.*, 2020, **59**, 9408–9413.
- J. Chen, H. Tang, M. Huang, Y. Yan, J. Zhang, H. Liu, J. Zhang, G. Wang and R. Wang, *ACS Appl. Mater. Interfaces*, 2021, **13**, 26960–26970.
- F. Ruan, F. Li, Z. Dong, Q. Ke, Y. Jin, W. Zhan, M. N. Ha and J. Tang, *Green Synth. Catal.*, 2021, **2**, 38–44.
- M. Koutani, E. Hayashi, K. Kamata and M. Hara, *J. Am. Chem. Soc.*, 2022, **144**, 14090–14100.
- Q. Ke, Y. Jin, F. Ruan, M. N. Ha, D. Li, P. Cui, Y. Cao, H. Wang, T. Wang, V. N. Nguyen, X. Han, X. Wang and P. Cui, *Green Chem.*, 2019, **21**, 4313–4318.
- Y. Pérez-Badell, X. Solans-Monfort, M. Sodupe and L. A. Montero, *Phys. Chem. Chem. Phys.*, 2010, **12**, 442–452.
- J. Oviedo and M. J. Gillan, *Surf. Sci.*, 2001, **490**, 221–236.
- Y. Hao, B. Liu, L. Tian, F. Li, J. Ren, S. Liu, Y. Liu, J. Zhao and X. Wang, *ACS Appl. Mater. Interfaces*, 2017, **9**, 12687–12693.
- J. Wang, X. Xu, Y. Liu, Z. Wang, P. Wang, Z. Zheng, H. Cheng, Y. Dai and B. Huang, *ChemSusChem*, 2020, **13**, 3488–3494.
- S. Tan, Y. Ji, Y. Zhao, A. Zhao, B. Wang, J. Yang and J. G. Hou, *J. Am. Chem. Soc.*, 2011, **133**, 2002–2009.
- M. Setvin, U. Aschauer, P. Scheiber, Y. Li, W. Hou, M. Schmid, A. Selloni and U. Diebold, *Science*, 2013, **341**, 988–991.
- M. Li, S. You, X. Duan and Y. Liu, *Appl. Catal., B*, 2022, **312**, 121419.
- X. Kang, G. Dong and T. Dong, *ACS Appl. Energy Mater.*, 2023, **6**, 1025–1036.
- Y. Zhuo, X. Guo, W. Cai, T. Shao, D. Xia, C. Li and S. Liu, *Appl. Catal., B*, 2023, **333**, 122789.
- M. Yang, K. Wu, S. Sun, J. Duan, X. Liu, J. Cui, S. Liang and Y. Ren, *ACS Catal.*, 2023, **13**, 681–691.
- J. Tang, Q. Zhang, K. Hu, P. Zhang and J. Wang, *J. Catal.*, 2017, **353**, 192–198.
- M. Liu, Q. Wang, Z. Liu, Y. Zhao, X. Lai, J. Bi and D. Gao, *Chem. Eng. J.*, 2020, **383**, 123161.
- P. V. Vardhan, M. B. Idris, H. Y. Liu, S. R. Sivakkumar, P. Balaya and S. Devaraj, *J. Electrochem. Soc.*, 2018, **165**, A1865.
- T. He, X. Zeng and S. Rong, *J. Mater. Chem. A*, 2020, **8**, 8383–8396.
- T. J. Frankcombe and Y. Liu, *Chem. Mater.*, 2023, **35**, 5468–5474.
- G. Qi, X. Liu, C. Li, C. Wang and Z. Yuan, *Angew. Chem., Int. Ed.*, 2019, **58**, 17406–17411.
- L. Liu, R. Liu, T. Xu, Q. Zhang, Y. Tan, Q. Zhang, J. Ding and Y. Tang, *Inorg. Chem.*, 2020, **59**, 14407–14414.
- S. Rong, K. Li, P. Zhang, F. Liu and J. Zhang, *Catal. Sci. Technol.*, 2018, **8**, 1799–1812.
- Y. Huang, Y. Liu, W. Wang, M. Chen, H. Li, S. Lee, W. Ho, T. Huang and J. Cao, *Appl. Catal., B*, 2020, **278**, 119294.
- F. Morales, D. Grandjean, A. Mens, F. M. F. Groot and B. M. Weckhuysen, *J. Phys. Chem. B*, 2006, **110**, 8626–8639.
- Y. Xu, J. Dhainaut, G. Rochard, J. Dacquin, A. Mamede, J. Giraudon, J. Lamonier, H. Zhang and S. Royer, *Chem. Eng. J.*, 2020, **388**, 124146.
- J. Tang, B. Jiao, W. Chen, F. Ruan, F. Li, P. Cui, C. Wan, M. N. Ha, V. N. Nguyen and Q. Ke, *Nano Res.*, 2022, **15**, 6076–6083.
- Y. Jin, F. Li, P. Cui, Y. Yang, Q. Ke, M. N. Ha, W. Zhan, F. Ruan, C. Wan, Z. Lei, V. N. Nguyen, W. Chen and J. Tang, *Nano Res.*, 2021, **14**, 2637–2643.
- Q. Ke, D. Yi, Y. Jin, F. Lu, B. Zhou, F. Zhan, Y. Yang, D. Gao, P. Yan, C. Wan, P. Cui, D. Golberg, J. Yao and X. Wang, *ACS Sustain. Chem. Eng.*, 2020, **8**, 5734–5741.



- 46 H. Li, Y. Zhang, J. Tang, G. Huang, P. Cui and Q. Ke, *Green Synth. Catal.*, 2022, DOI: [10.1016/j.gresc.2022.09.005](https://doi.org/10.1016/j.gresc.2022.09.005).
- 47 J. Yu, T. Zeng, H. Wang, H. Zhang, Y. Sun, L. Chen, S. Song, L. Li and H. Shi, *Chem. Eng. J.*, 2020, **394**, 124458.
- 48 H. Li, J. Shang, Z. Ai and L. Zhang, *J. Am. Chem. Soc.*, 2015, **137**, 6393–6399.
- 49 Y. Lin, Z. Liu, L. Yu, G. Zhang, H. Tan, K. Wu, F. Song, A. K. Mechler, P. P. M. Schlekler, Q. Lu, B. Zhang and S. Heumann, *Angew. Chem., Int. Ed.*, 2021, **60**, 3299–3306.
- 50 F. Li, J. Tang, Q. Ke, Y. Guo, M. N. Ha, C. Wan, Z. Lei, J. Gu, Q. Ling, V. N. Nguyen and W. Zhan, *ACS Catal.*, 2021, **11**, 11855–11866.
- 51 J. Li, X. Wang, J. Tian, X. Zhang and F. Shi, *Rare Met.*, 2023, **42**, 1877–1887.
- 52 B. He, H. Jin, Y. Wang, C. Fan, Y. Wang, X. Zhang, J. Liu, R. Li and J. Liu, *Rare Met.*, 2022, **41**, 132–143.
- 53 N. Siemer, A. Lüken, M. Zalibera, J. Frenzel, D. Muñoz-Santiburcio, A. Savitsky, W. Lubitz, M. Muhler, D. Marx and J. Strunk, *J. Am. Chem. Soc.*, 2018, **140**, 18082–18092.
- 54 T. Xia, W. Gong, Y. Chen, M. Duan, J. Ma, X. Cui, Y. Dai, C. Gao and Y. Xiong, *Angew. Chem., Int. Ed.*, 2022, **61**, e202204225.

